AIAA SciTech Forum
13-17 January 2014, National Harbor, Maryland
52nd Aerospace Sciences Meeting

10.2514/6.2014-0903

Multipoint Aerodynamic High Fidelity Shape Optimization of an Isolated Engine Nacelle

H. Toubin[1], I. Salah El Din[2] and M. Meheut[3]
Onera, The French Aerospace Lab, Meudon, France

The optimization of an isolated civil aircraft generic engine nacelle is presented in this paper using multi-point and up-to-date analysis and optimization tools. Opposite to components such as aircraft wing design, more limited material can be found on nacelle optimal aerodynamic design. The present work aims at describing a first step toward building a methodology complying with constraints which are specific to engine industrial design using high fidelity CFD approaches. Two critical design points, cruise and cross-wind, are considered separately and then concurrently using efficient local and global optimization algorithms.

Nomenclature

AoA	=	angle of attack
a_n	=	design variable α lower bound
B	=	wall boundaries (skin, inflow and outflow)
b_n	=	design variable α upper bound
C_p	=	pressure coefficient
C_L	=	lift coefficient
C_{D_p}	=	pressure drag coefficient
$\vec{\imath}$	=	streamwise normal vector
CDI	=	Circumferential Distortion Index
J	=	objective function
M_∞	=	free stream Mach number
$\vec{n}$	=	boundary normal vector
$\bar{p}$	=	mean stagnation pressure
p_i	=	stagnation pressure on crown probe
P_i	=	control points in the vertical sections
Q_i	=	control points in the horizontal sections
S_{ref}	=	reference non dimensioning surface
u_∞	=	free stream velocity
α	=	aerodynamic design variable
ρ_∞	=	free stream density
ϵ	=	ratio between the infinite streamtube and the nacelle intake cross-sections

[1] PhD Student, *Applied Aerodynamics Department*, Helene.Toubin@onera.fr.
[2] Dr. Research Engineer, *Applied Aerodynamics Department*, Itham.Salah_El_Din@onera.fr.
[3] Dr. Research Engineer, *Applied Aerodynamics Department*, Michael.Meheut@onera.fr.

I. Introduction

IN the current airframe design context, every component is expected to be always better performing from one generation to the next. In particular, engines are required to reach maximal efficiency for targeted ranges. In order to minimize the penalty on the overall performance, every sub-component must undergo careful design effort. The nacelles are meant to enhance the aerodynamic performance as well as to reduce the noise in the cabin or at ground-level. Nacelle design is usually a difficult, iterative process, representing a time-consuming step in an engine design process. Nacelle designers must indeed deal with multiple constraints which can be structural, thermal, concerning mass or integration of the engine elements, as well as radically different flow conditions during the various flight stages. Among the different design methods available, optimization methods can allow a fast, robust and efficient design process.

This paper presents the work performed to build up a methodology to solve an optimization problem meant to enhance an isolated engine nacelle aerodynamic performance at two critical flow conditions. To our knowledge, little information is available in the literature on aerodynamic multipoint optimization of nacelles. Recent work has been performed by Song and Keane[1] on aero-acoustic optimization using a stochastic algorithm on CFD-based surrogate response models. Sasaki and Nakahashi[2] have conducted single cruise condition optimization under geometrical constraints over-the-wing nacelle optimizations also based on stochastic optimization algorithms combined with Euler CFD based surrogate models. Lambert et al.[3] solved a constrained optimization problem with gradient-based algorithms, the gradients being calculated using the optimal control theory and sensitivity analysis approaches. An original approach using an inverse design approach developed originally by Takanashi[4] has also been recently proposed by Wilhelm[5]. No reference to a multi-point optimization was found in the literature. The approaches which are considered in the present study have already been thoroughly used for aerodynamic wing design problems[6,7]. They are applied to a reference nacelle based on the DLR-F6 geometry provided in the Drag Prediction Workshop 3 (DPW3)[8]. The main challenge in isolated nacelle design lies in the ability to improve the performance at multiple flow conditions while taking into account the engine behavior through the geometry and the inflow condition modifications. Among the different flow conditions encountered during a flight, three are considered critical: take-off, cross-wind and cruise condition. Take-off condition will not be discussed in this study for reasons explained in the following section.

One of the requirements to achieve a successful optimization for such problems is therefore to reach a tradeoff between accuracy and robustness of the nacelle performance assessment. The targeted problem will tackle the multi-point optimization aspects at frozen engine conditions. In cruise condition drag minimization is the targeted function of interest whereas in cross-flow condition, separation is to be avoided and the circumferential distortion index is considered.

The problem definition, including the reference configuration and the optimization problem formulations will be thoroughly presented. The analysis framework providing the performance as well as its sensitivity, when needed, to the design parameters will also be described in detail. Finally, the results of the various optimizations will be analyzed and the resulting know-how on nacelle optimization acquired through this study will be extracted.

II. Multipoint aerodynamic optimization problem

A. Reference geometry and aerodynamic design conditions

The chosen baseline is the DLR-F6 nacelle geometry. As shown in Figure 1(a), the nacelle is equipped with a compressor and turbine plane respectively as outflow and inflow surfaces. Considering the available data, it was decided to use a simplified geometry, without any fan or central body component. A structured multiblock mesh of 2 million points has been generated using ICEM-Hexa mesher (cf. Figure 1 (a) and (b)) around the nacelle and adapted to RANS CFD computation requirements, especially at the vicinity of the nacelle skin.

The geometry is dimensioned for 1:1 scale conditions. The dimensioning was found using the scales of the Airbus A300. Its length is 6.88 m, the diameter of the fan is 2.11 m, the air intake has a diameter of 2.12 m and the maximum width of the nacelle is 2.90 m. The reference surface chosen for the global coefficient calculations is set to $S_{ref} = 102.56$ m^2 (half aircraft configuration reference surface).

For aircraft certification, three critical flight conditions are considered: cruise, take-off and cross-wind. The performance of the reference nacelle was assessed in the three conditions, but the take-off one was not kept for the optimization problem since a strong flow separation occurred outside the nacelle, causing numeric reliability problems. Cruise and cross-wind conditions are described in section IV.

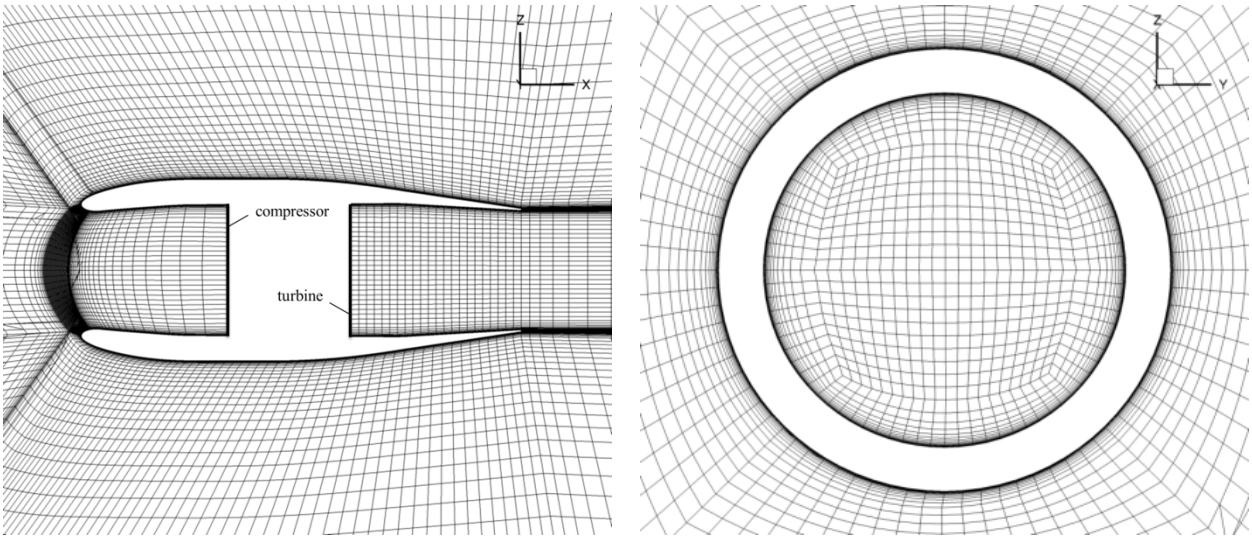

(a) Streamwise cut (b) Cross cut

Figure 1. Modified DLR-F6 geometry and mesh planes

B. Optimization problem formulation

The optimization problem consists in finding the set of design parameters, which will minimize both drag at single cruise condition and flow separation under crosswind condition for an isolated engine nacelle. The multi-point optimization method is achieved in two sequential steps.

The first step of this work consists in defining and separately achieving two mono-objective optimization problems, for cruise and crosswind conditions. The topic of the parameterization will be discussed in a dedicated following section.

For the cruise design point, the chosen objective function is the pressure drag coefficient C_{D_p} formulated in Equation (1) although viscous drag components are available as RANS computations are performed. This choice is mainly motivated by the fact that the wetted surface, and thus the associated friction drag, of the nacelle is only marginally modified.

$$C_{D_p} = \frac{2}{\rho_\infty u_\infty^2 S_{ref}} \int_B (p - p_\infty) \vec{n}.\vec{i}\, dS \tag{1}$$

The optimization problem is thus expressed as follows:

$$J_1 = \min_\alpha \left(C_{D_p}(\alpha) \right) \text{ such that } a_n \leq \alpha_n \leq b_n \tag{2}$$

where α_n are the design variables allowed to vary within the range [a_n,b_n].

For the crosswind design point, the interesting feature of the flow is the distortion index which quantifies the flow separation inside the nacelle air intake. The Circumferential Distortion Index[9] (CDI) is used. 40 numerical pressure probes located as seen in Figure 2(a) allow to define the CDI:

$$CDI = \max_{1 \leq i \leq \text{nradius}-1} \left(0.5 \left(\frac{\bar{p}_i - p_{min_i}}{\bar{p}} + \frac{\bar{p}_{i+1} - p_{min_{i+1}}}{\bar{p}} \right) \right) \tag{3}$$

where $\bar{P}$ is the mean stagnation pressure over all the probes, $\bar{p}_i$ over the crown *i* among nradius crowns and p_{min_i} is the minimum stagnation pressure on the crown *i*. The optimization problem reads now:

$$J_2 = \min_\alpha \big(CDI(\alpha) \big) \text{ such that } a_n \leq \alpha_n \leq b_n \tag{4}$$

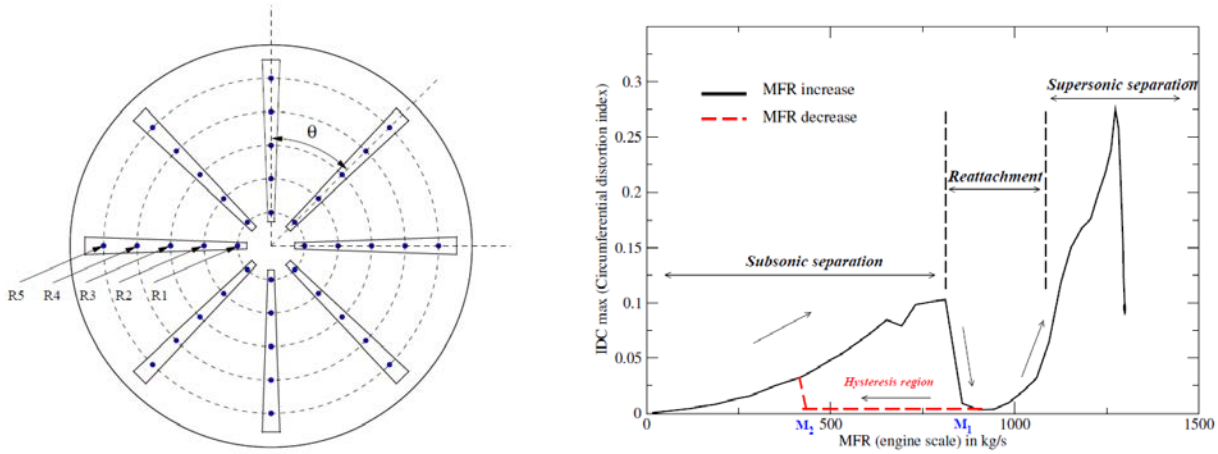

(a) Pressure probe distribution in the control plane (b) Typical CDI evolution with respect to mass flow rate

Figure 2. CDI definition and behaviour (figures from Colin & al.[9])

The second step consists in combining the two mono-objective problems in order to get a bi-objective and bi-point optimization problem. There are now two independent objective functions and one must find the sets of parameters α which will give the best trade-off between C_{D_p} and CDI:

$$(J_1, J_2) = \min_\alpha \left(C_{D_p}(\alpha), CDI(\alpha) \right) \text{ such that } a_n \leq \alpha_n \leq b_n \quad (5)$$

The parameterization must now be described in order to define completely the optimization problem.

C. Parameterization

In order to deform the nacelle without changing the engine conditions, the nozzle will be kept unchanged in the whole optimization process. To deform the remaining geometry of the nacelle, four azimuthal control sections are used to parameterize the nacelle shape definition: at θ=0°,90°,180°,270° azimuth angle positions for all optimization problems considered, with five B-spline type control points P_i in each section, as illustrated in Figure 3. Three are located on the outer surface respectively at 25, 50 and 75% of local chord length, one pilots the leading edge radius and a single one pilots the inner surface near the leading edge.

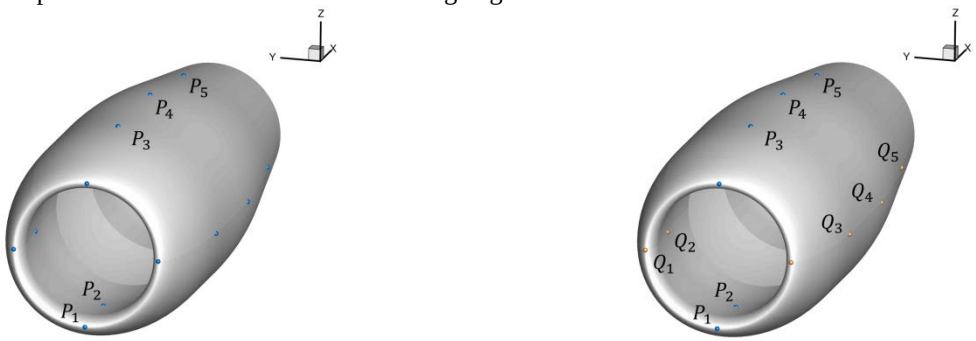

(a) Cruise optimization (b) Cross flow optimization

Figure 3. Nacelle parameterization for the optimization problems considered

For the cruise only optimization, the control point displacements are identical in each of these control sections, resulting in an axisymmetric geometry. For the cross-flow and the multi-objective optimizations, the control points P_i in the vertical plane sections ($\theta = 0°, 180°$) share the same displacements but can be displaced differently from the control points Q_i in the horizontal plane sections ($\theta = 90°, 270°$).

The upper and lower bounds are chosen so as to conserve the quality of the mesh in the vicinity of the skin, especially to avoid negative cells. They are defined in table 1.

	(P_1, Q_1)	(P_2, Q_2)	(P_3, Q_3)	(P_4, Q_4)	(P_5, Q_5)
Lower bound	-0.1	-0.05	-0.5	-0.4	-0.2
Upper bound	0.05	0.05	0.1	0.1	0.1

Table 1. Upper and lower bounds for each control point displacement

Each of the afore mentioned optimization problem has been implemented within an automated optimization framework. In the following section, this framework is described in detail from the global optimization process to the performance analysis.

III. Aerodynamic engine nacelle optimization process description

A. Overall optimization system architecture

The optimization process can be decomposed into two main components: the optimizer in which are embedded the various optimization algorithms and the analyzer which is meant to assess single geometry performance and sensitivity calculations, as shown in Figure 4.

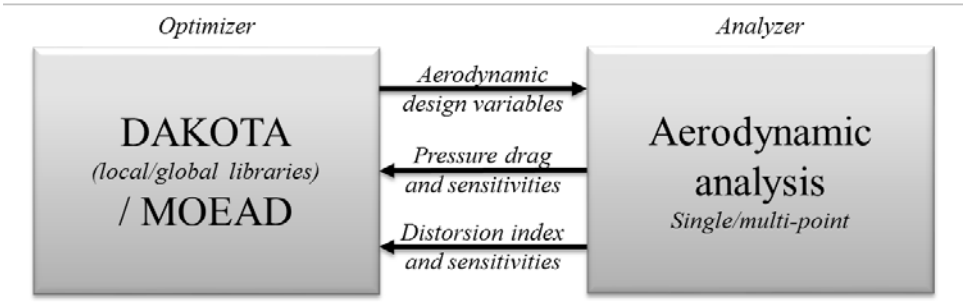

Figure 4. Global optimization process structure

The optimizer provides the analyzer with the design variables set, describing a new better performing geometry to be analyzed, to be computed. Local (gradient-based DOT[10] algorithm) optimization algorithm coupled with DAKOTA[11] has been used for the single point optimizations. Gradients have been computed either with finite differences or adjoint methods for the cruise point. CMA-ES[12] (*Covariance Matrix Adaptation Evolutionary Strategy*) has also been used for the mono-objective optimizations. For the two-point optimization the MOEA/D (*Multiobjective Evolutionary Algorithm / Decomposition*)[13] algorithm-based tool has been used to generate the pareto front of the optimal solution family.

B. Analyzers architecture

For a new set of aerodynamic shape parameters, the ONERA in-house SeAnDef (*Sequential Analytical Deformation*) analytic approach is used to deform the CFD mesh and to adapt it to the new shape. The mesh deformation tool is based on user-defined control points and sections. The upper and lower bounds for each control point are user defined. Initially developed for wing deformation, it has undergone an extension to isolated nacelle shape deformations. The available deformation modes which can be combined are chord length, twist, translation, thickness, camber and profile deformations. The deformations defined by the user at the control points are interpolated on the whole skin before being propagated into the entire mesh. Once the mesh is deformed, RANS aerodynamic calculations are completed with the ONERA elsA[14] code. The following CFD post processing enables the drag or distortion index extraction as well as their sensitivities with respect to the design variables. The overall process is illustrated in Figure 5 for the single optimization processes and in Figure 6 for the two-point optimization. Both direct and gradient-based process architectures are illustrated.

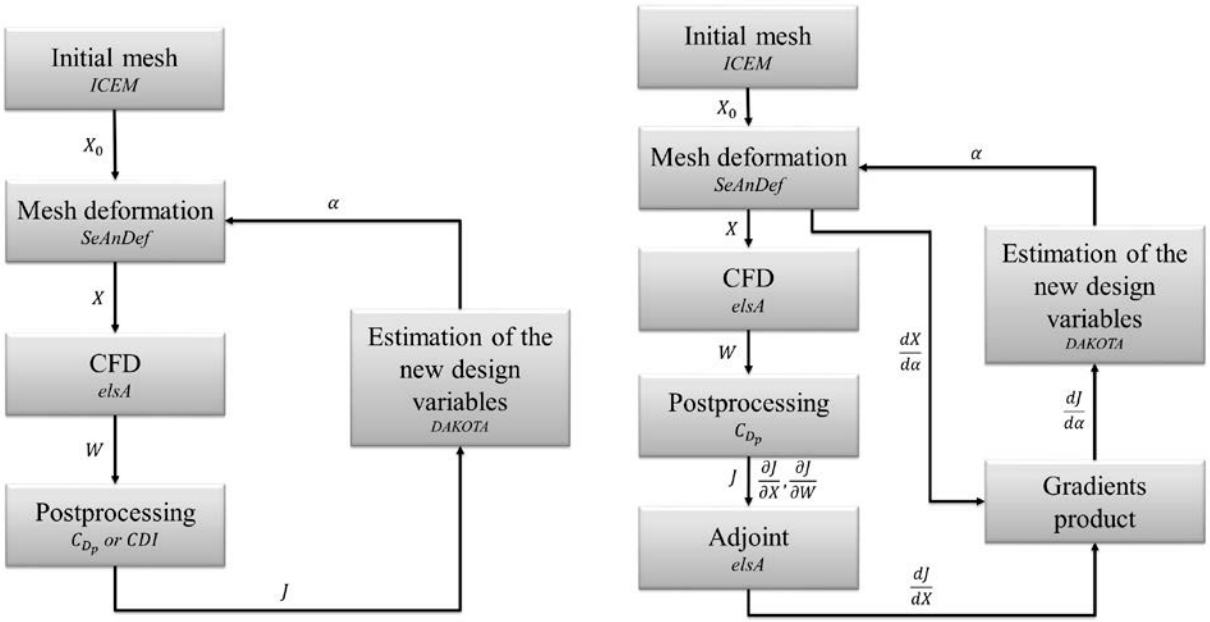

(a) Direct performance analysis process (b) Gradient based process

Figure 5. Single objective analyzer architecture

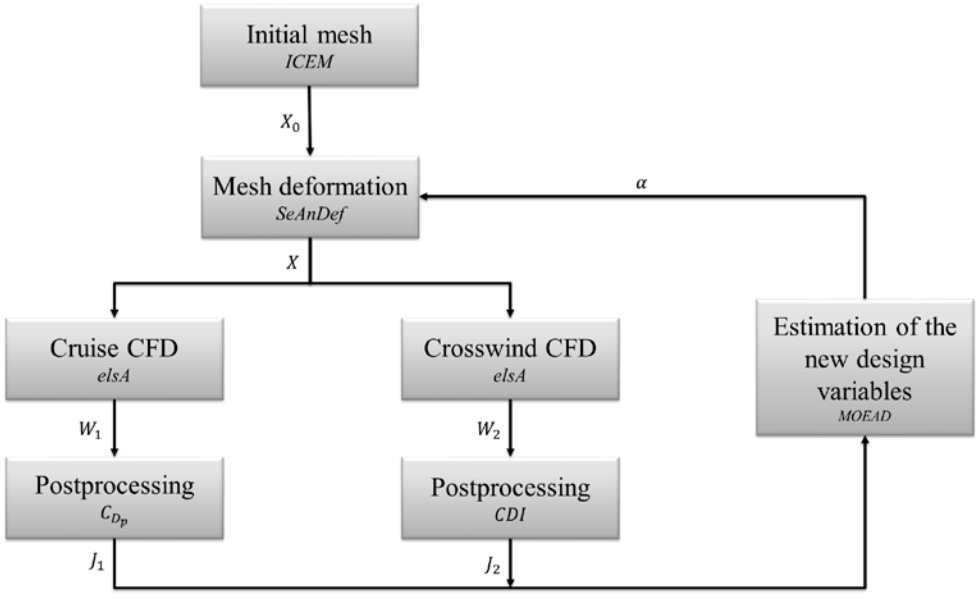

Figure 6. Two-objective optimization process

C. Sensitivities calculation

The sensitivities of the functions of interest with respect to the design variables have been computed using two approaches. The first one is the usual finite difference and the second one is based on the adequate adjoint problem resolution. The finite difference is mandatory for the evaluation of the sensitivities of CDI as the function can hardly be linearized as it is formulated in equation (3). On the other hand, the pressure drag coefficient sensitivities using

the adjoint approach is available and its use has already been demonstrated throughout previous optimization studies[6,7]. The discrete adjoint formulation is adopted in the elsA solver[15] and is meant to calculate the gradients from (6).

$$\nabla_\alpha J(\alpha) = \frac{\partial J}{\partial X}\frac{dX}{d\alpha} + \frac{\partial J}{\partial W_b}\frac{dW_b}{dX}\frac{dX}{d\alpha} + \lambda_a^T \frac{\partial R_a}{\partial X}\frac{dX}{d\alpha} \tag{6}$$
$$\left(\frac{\partial R_a}{\partial W}\right)^T \lambda = -\left(\frac{\partial J}{\partial W_b}\frac{\partial W_b}{\partial W} + \frac{\partial J}{\partial W}\right)^T$$

where J can be an objective function as well as a constraint. The aerodynamic drag coefficients depend on the mesh but also on the flow field W as well as the boundary conditions W_b. The sensitivities of the mesh with respect to the design variables is provided by the external mesh deformation module whereas the J function sensitivities with respect to the flow and the mesh is provided by the CFD post-processing module embedded in the far field drag extraction tool ffd72[16]. The elsA/Opt adjoint solver is dedicated to RANS adjoint computation with frozen eddy viscosity assumption in the present study.

IV. Performance of the reference configuration

A preliminary study of the reference configuration performance has been carried out. The analysis of the results is aimed at defining suitable numerical settings for the CFD calculation which will be used in the optimization processes.

A. Cruise conditions

The aerodynamic conditions chosen for this point are a Mach number of 0.82 for a flight altitude of 35,000 ft. with zero angle of attack corresponding to a Reynolds number of 6.5 10^6. The flow rate was imposed through a static pressure condition on the compressor plane, and a stagnation pressure condition was imposed on the turbine plane. The incoming flow rate was chosen so as to have a ratio ϵ between the infinite streamtube and the nacelle intake cross-sections equal to 0.7. It gives a flow rate of 227.5 kg/s, and a corresponding static pressure of 32,690.54 Pa. The stagnation pressure in the turbine plane is equal to 1.5 times the reference stagnation pressure: 56,073.95 Pa.

Figure 7(a) show the convergence of two state variables as well as the streamwise flux. 2,000 iterations are sufficient to get a flow field converged enough for optimization purposes. Even though the L_2 normed residuals do not drop significantly, the global flux performance deviation is lower than 0.1 drag count between 2,000 and 20,000 iterations. The reference design has been analyzed at cruise conditions and reaches a pressure drag C_{D_p} of 51.39 drag counts. The aim of the optimization is to reduce the supersonic region on the outer surface near the leading edge which appears in Figure 7(b), from which originates a wave pressure drag contribution.

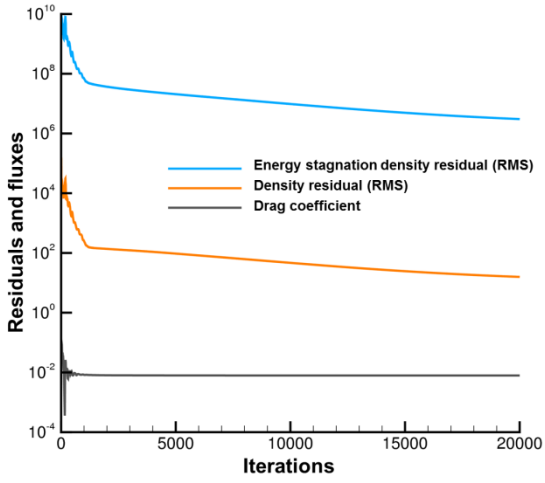

(a) Convergence curves

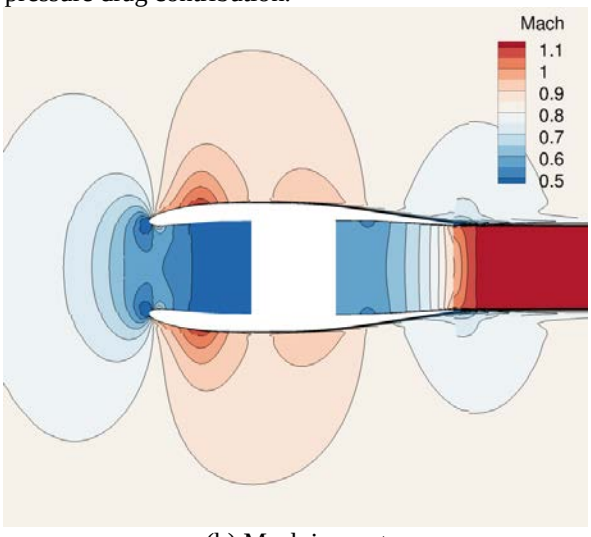

(b) Mach isocontours

Figure 7. Reference nacelle flow and computation convergence at cruise condition

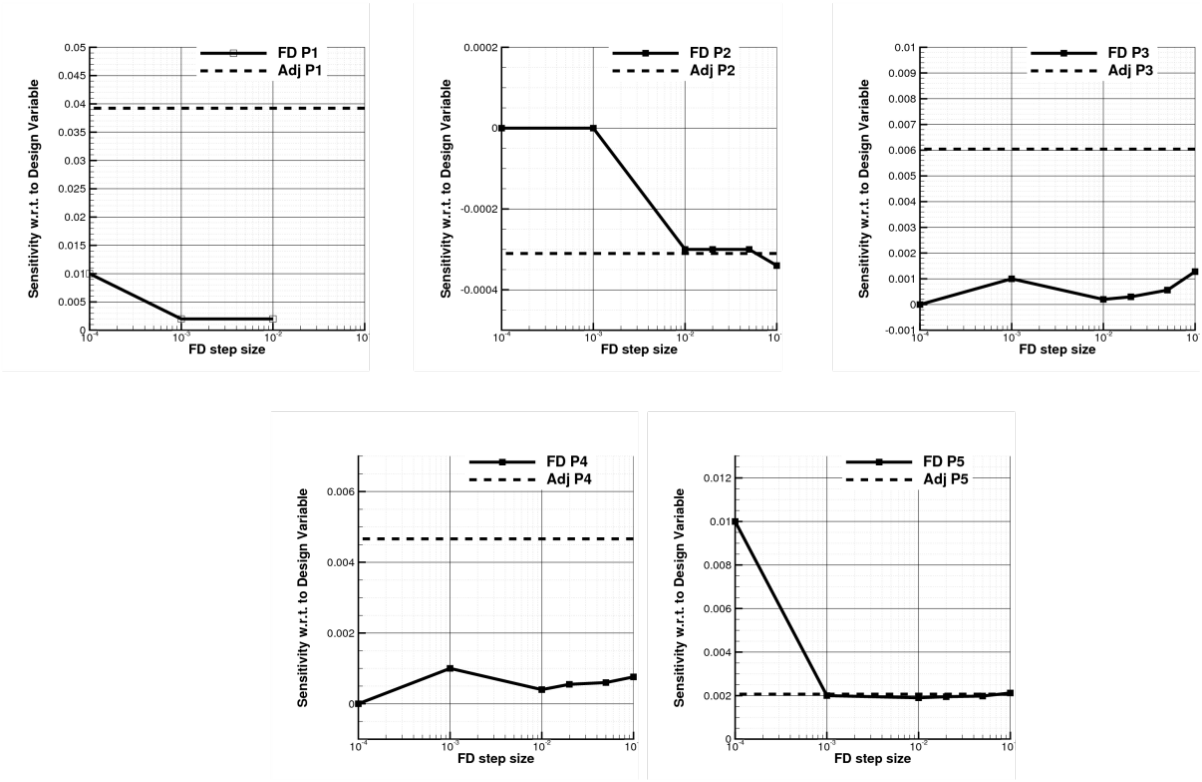

Figure 8. Finite difference and Adjoint based sensitivities comparison

The use of gradient-based optimization algorithms calls for preliminary sensitivity validation. In the case of finite differences a discretization step needs to be defined. In the present study the sensitivities obtained with various step sizes are compared with the one obtained using the adjoint approach on the reference geometry for the prescribed parameterization. The results are provided in Figure 8. Although all calculated gradients show consistent sign with the adjoint based gradient, only the second and fifth variables gradients reach the same amplitude. A step of 10^{-2} is suitable to initiate the optimization process based on finite difference gradients. However, adjoint based gradients will be more reliable, even to solve the optimization considered in this study with a limited number of design variables.

B. Crosswind conditions

For the crosswind condition, the flow is taken at the ground level atmospheric conditions, with a Mach number set at 0.05 (equivalent to a wind of 20 kt) and a sideslip angle of 90°. The flow rate has a large influence on the distortion inside the nacelle as seen in Figure 9(a). The mass flow rate chosen for the optimization is 400 kg/s since the separation is then subsonic, therefore more numerically robust. It corresponds to an $\epsilon = 5.6$ and is equivalent to a static pressure of 95,802.79 Pa. The stagnation pressure on the turbine plane is 152,253.65 Pa.

The convergence curves are shown in Figure 9(b). The residuals are not very well converged, due to the flow separation at the leading edge. However the fluxes are well converged and the CDI varies only of 10^{-3} between 2,000 and 20,000 iterations, so that 2,000 iterations are used for the optimization.

Two turbulence models have been studied to ensure the validity of the CDI calculation (see Figure 9(b)), with the knowledge that none is able to capture the flow reattachment. This phenomenon has already been pointed out in literature [9]. For the optimization process, Menter k-ω SST model is chosen since it provides better prediction for separated flows. The reference design is such that a strong separation appears inside the intake of the nacelle as seen in Figure 10. A pair of vortices is visible in Figure 10(c). The distortion could therefore be reduced by reattaching the flow inside the air intake through a suitable design.

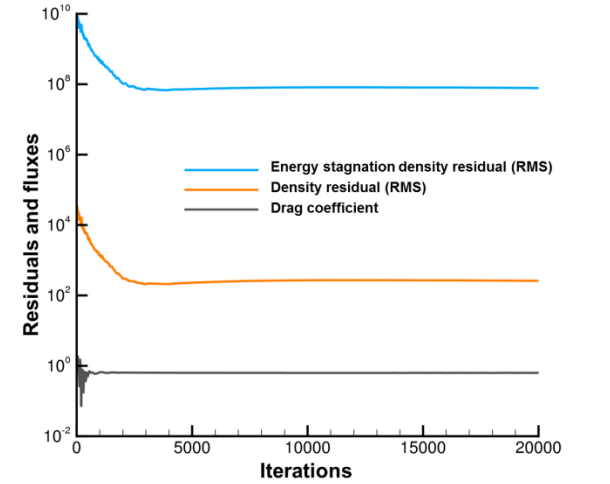

(a) Convergence curves

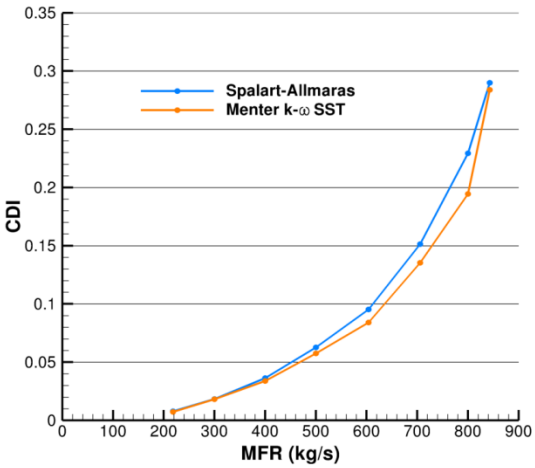

(b) CDI evolution with respect to mass flow rate for two turbulence models

Figure 9. Reference nacelle performance and computation convergence at cross flow conditions

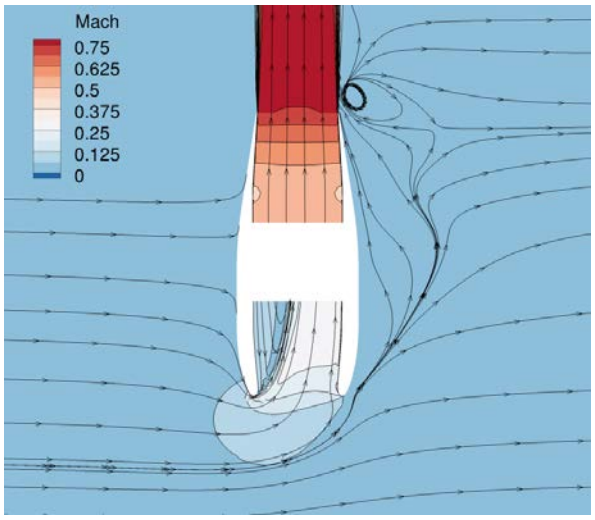

(a) Mach isocontours and streamlines

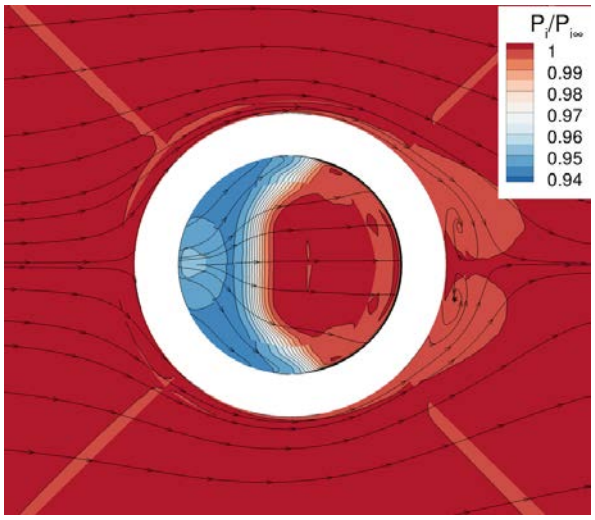

(b) Distortion and streamlines

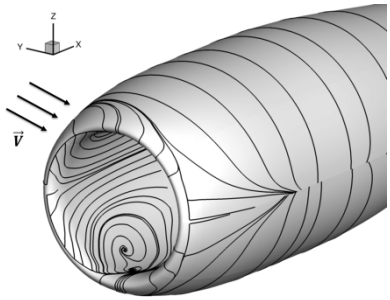

(c) Friction lines on the skin

Figure 10. Flow analysis of the reference nacelle at cross flow conditions

V. Optimization results

The two mono-objective optimizations have been performed first, giving antagonist results and interesting reference designs for the bi-point optimization.

A. Cruise optimization

The engine nacelle has first been optimized in cruise conditions, using two gradient-based methods and one genetic algorithm. The three methods give almost the same performance with similar optimal parameters, but with various restitution times.

1. Convergence

The convergence of the three optimization algorithms can be seen in Figure 11. The number of optimizer iterations has been non-dimensioned in order to compare the three algorithms. All three algorithms converge efficiently towards their optimal design. The convergence of the objective function, the pressure drag, is seen in Figure 12(a) and is also quite satisfactory.

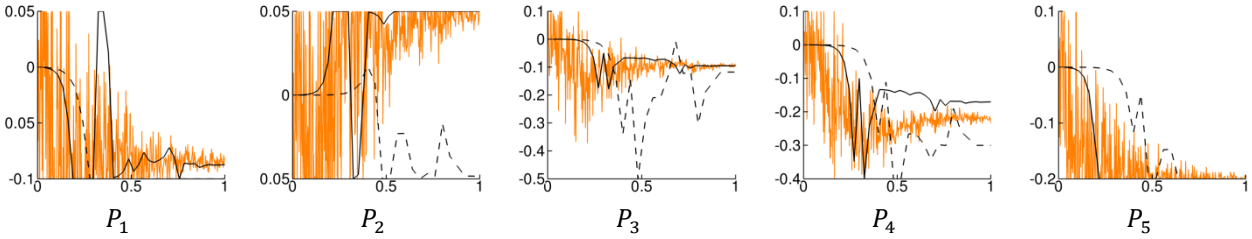

Figure 11. Convergence of the design variables for the cruise optimizations: finite differences based gradient (solid black), adjoint based gradient (dashed black) and CMA-ES (orange)

2. Optimal geometry

The optimal geometries are described in Table 1. Gradient based on finite differences and CMA-ES find almost the same geometry, with a slight advantage in terms of performance for CMA-ES. It is not surprising since CMA-ES explores a much larger variable range. Adjoint-based gradient method however fails in finding the global optimum, especially regarding the point P_2. This result is consistent with the error on the gradient computed by the adjoint found in section IV.A. Concerning the restitution times, the adjoint method required 25 evaluations or 50 CFD computations (direct and adjoint CFD), the finite differences approach 37 and CMA-ES 454.

	P_1	P_2	P_3	P_4	P_5	ΔC_{D_p}	Number of CFD evaluations
Finite Differences	-0.087	**0.05**	-0.095	-0.170	**-0.2**	-8.45%	37
Adjoint	**-0.1**	-0.048	-0.117	-0.300	**-0.2**	-7.41%	50
CMA-ES	-0.086	**0.05**	-0.100	-0.222	**-0.2**	-8.50%	454

Table 1: Optimal design variables and performance of the cruise optimization

The Figure 12(b) shows the corresponding nacelle geometries. Finite differences approach and CMA-ES profiles are quite similar, CMA-ES being thinner. The geometry obtained with the adjoint method is even thinner but loses drag performance due to the air intake design.

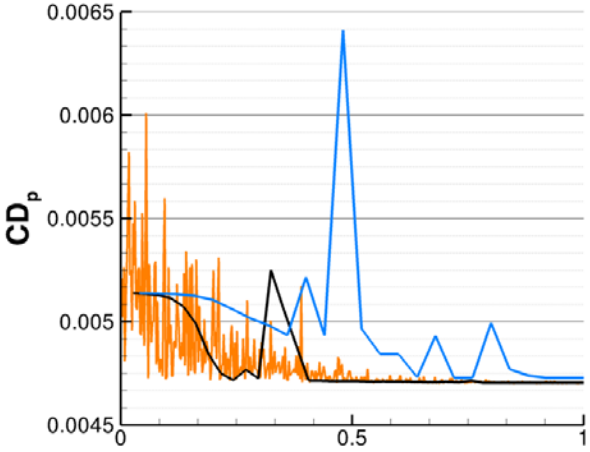

(a) Convergence of the objective function for the cruise optimization (black: DOT with finite differences, blue : DOT with adjoint, orange: CMA-ES)

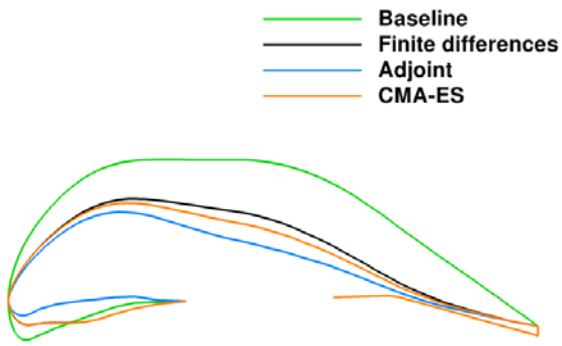

(b) Nacelle profiles

Figure 12. CD_p history and nacelle profiles of the cruise optimization results

3. Performance of the optimum

The performance of the optimal design achieved by CMA-ES is analyzed in Figure 13. The supersonic zone on the outer surface of the nacelle is reduced, which explains the pressure drag reduction.

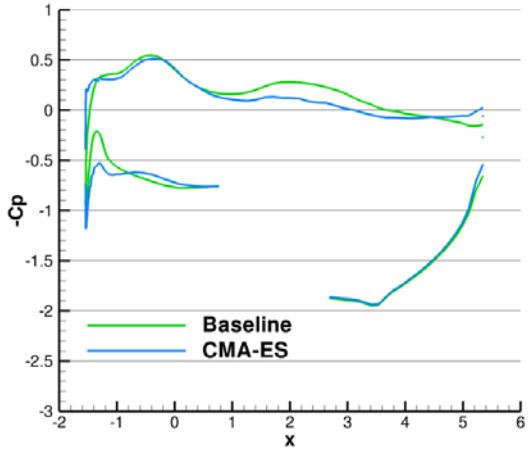

(a) Cp curves

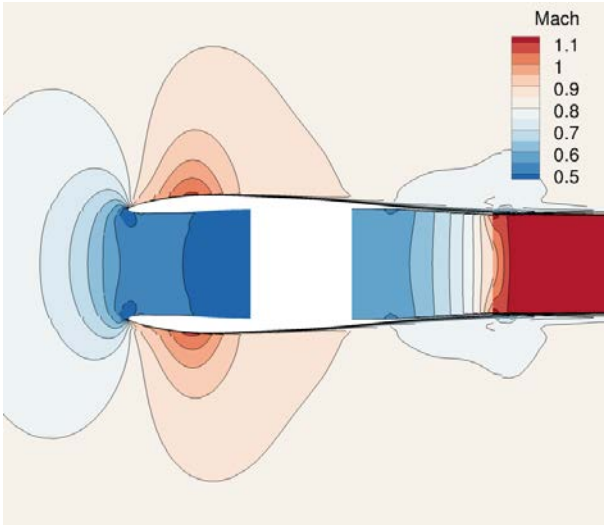

(b) Mach isocontours of the optimal geometry (CMA-ES)

Figure 13. Results of the cruise optimization

B. Cross-wind optimization

The adjoint-based method was not available for the cross-wind optimization process, since the evaluation of CDI is not linearized. Two methods were therefore used: gradient with finite differences and genetic algorithm. One must keep in mind that the parameterization now uses ten control points in two independent sections.

1. Convergence

The convergence of both algorithms is satisfactory (Figure 14). The finite differences seem to converge towards a local minimum and miss the 'global' optimum found by CMA-ES. However both methods succeed in reducing the distortion index by about 6% (see Figure 15 (a)).

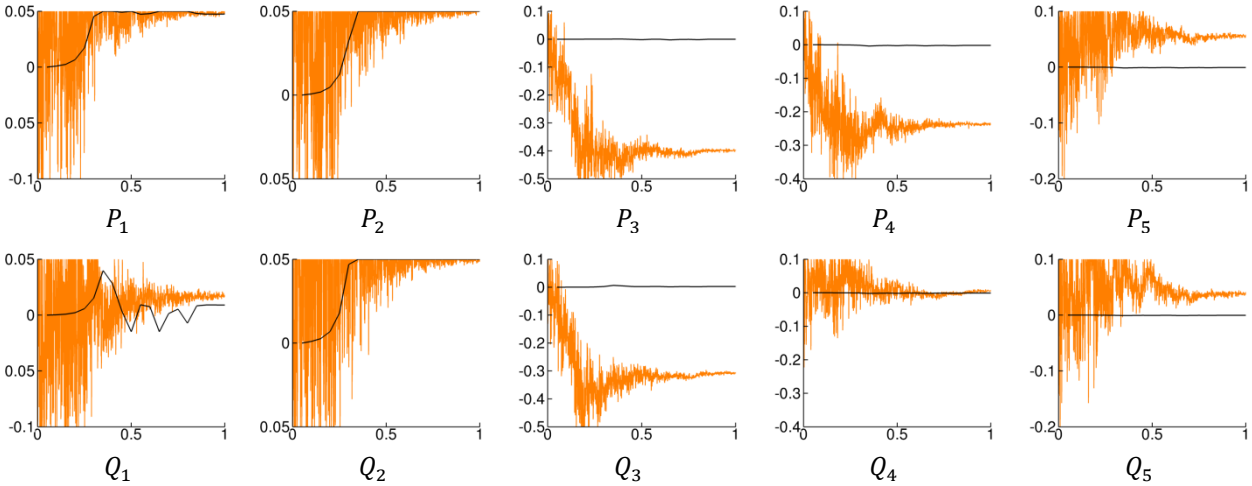

Figure 14. Convergence of the design variables for the cross-wind optimizations: finite differences (black) and CMA-ES (orange) (Control point displacements w.r.t non dimensioned iteration range)

2. Optimal geometry

The optimal design variables for both optimization methods are summarized in Table 2. Variables P_2 and Q_2, which correspond to the points inside the air intake, reach the upper bound. The corresponding profiles are plotted in Figure 15. They are quite different on the outer side of the nacelle, although the inside is almost similar for both optimizations, which explains the similar performance. It is consistent with the sensitivity analysis which has shown that the three points on the extrados are of small impact on the distortion index. It is also remarkable that the nacelle remains almost symmetric although the flow is completely dissymmetric.

	(P_1, Q_1)	(P_2, Q_2)	(P_3, Q_3)	(P_4, Q_4)	(P_5, Q_5)	ΔCDI	Number of CFD evaluations
Finite Differences	0.047, 0.009	**0.05**, **0.05**	0, 0.002	-0.002, -0.001	-0.001, 0	-5.46%	80
CMA-ES	0.049, 0.017	**0.05**, **0.05**	-0.400, -0.306	-0.239, 0.006	0.055, 0.040	-6.03%	973

Table 2: Optimal design variables and performance of the cross-wind optimization

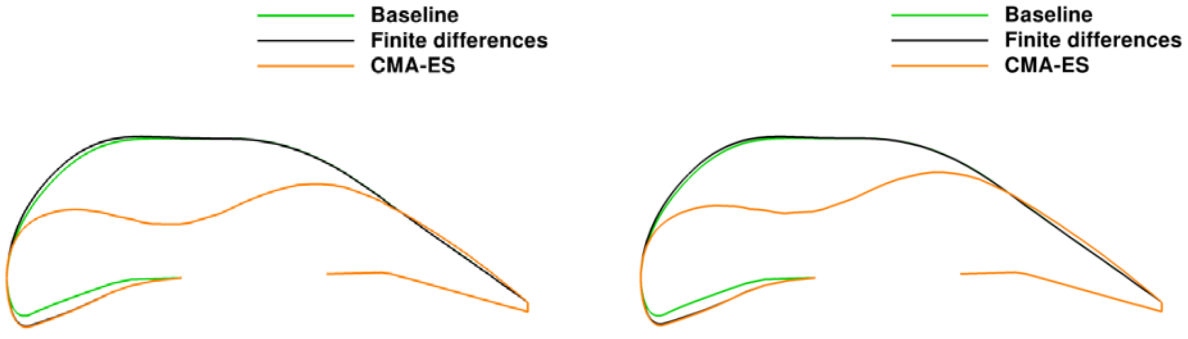

(a) Vertical profiles (θ=0° and 180°) (b) Horizontal profiles (θ=90° and 270°)

Figure 15. Bi-objective isolated nacelle optimization with MOEA/D

3. Performance of the optimum

The best design found by the two optimizations is analyzed in Figure 16. The separation is reduced and the pair of vortices has turned into a single vortex (see Figure 16(d)) which explains the better performance in terms of distortion.

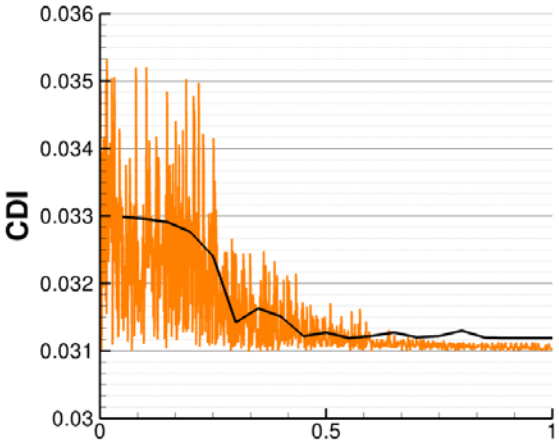

(a) Convergence of the objective function
for the cross-wind optimization
(black: finite differences, orange: CMA-ES)

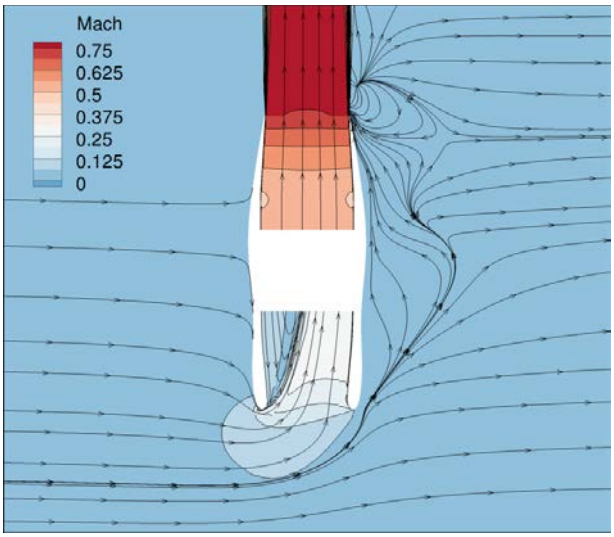

(b) Mach isocontours
of the optimal geometry (CMA-ES)

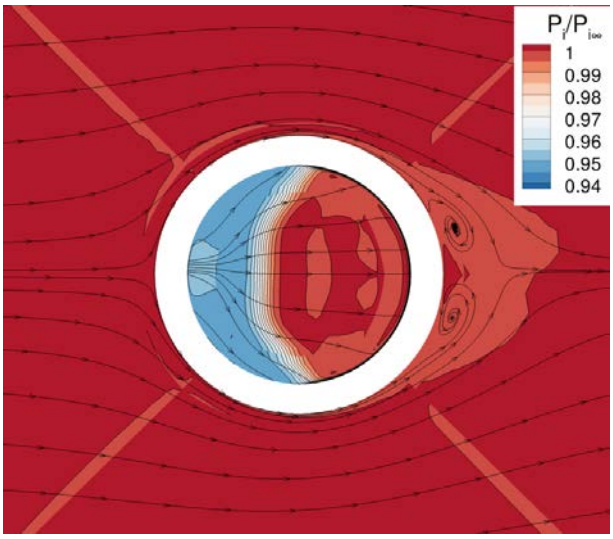

(c) Distortion isocontours
of the optimal geometry (CMA-ES)

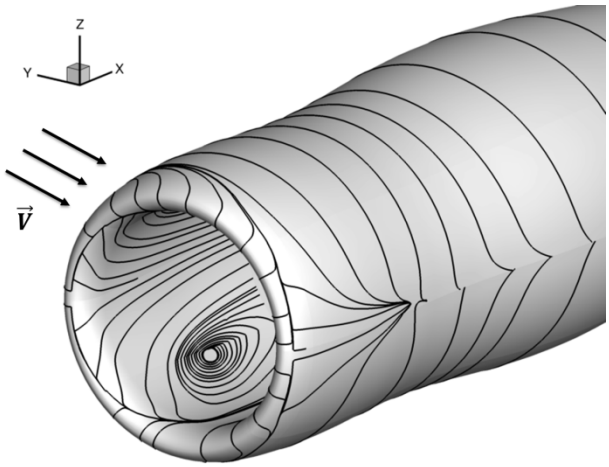

(d) Friction lines
on the optimal geometry (CMA-ES)

Figure 16. Results of the cross-wind optimization

The conclusion of the two mono-objective optimization is that both designs and performance illustrate the antagonism of the problems (see single objective problems performance results in Figure 17) and therefore a designer cannot optimize a nacelle for only one condition and get a realistic design. A bi-point optimization is therefore carried out in order to find out if an optimizer is capable of finding a good trade-off.

C. Bi-objective optimization

1. Convergence

The complete bi-objective optimization has been run with the MOEA/D[12] evolutionary algorithm for five generations and the resulting generation performance is summarized in Figure 17. The baseline and the initial geometry performance are recalled as well as the single objective optimization optimum ones and significant performance enhancement possibilities are shown for both conditions. The pareto front clearly appears after 4 generations, providing a set of geometries opening the choice for the best trade-off between both conditions. The increase in the number of generation has not shown significant improvement in the description of the pareto front considering the initial population sizing which was chosen.

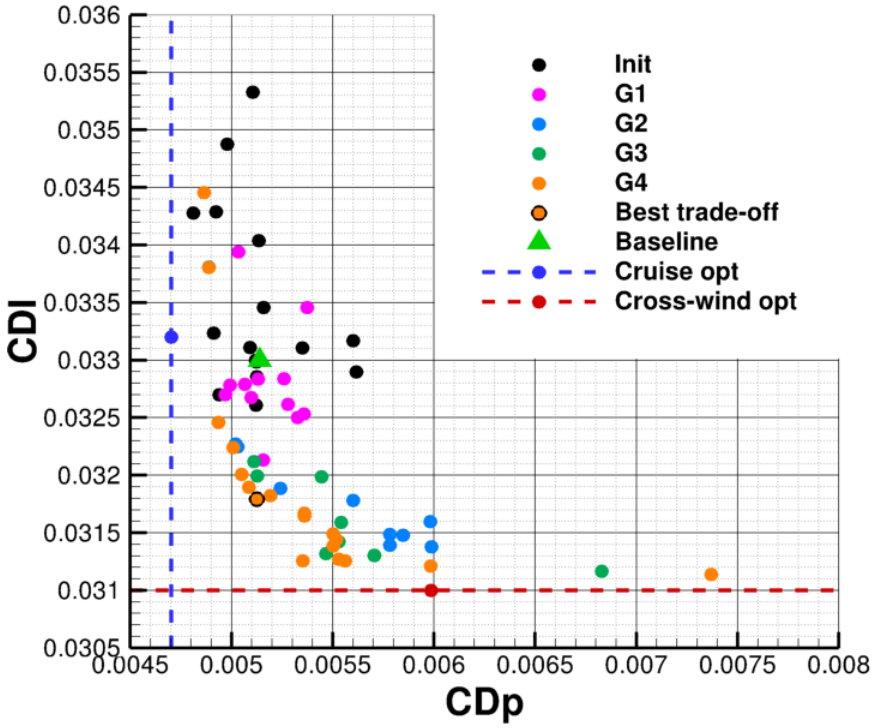

Figure 17. Bi-objective isolated nacelle optimization with MOEA/D

2. Best trade-off geometry

Table 3 summarizes the geometry and performance of the best trade-off geometry given in Figure 17, defined as the design performance closest to an equal weighting of each objective function. The profiles resulting from the three optimizations are also shown in Figure 18. The trade-off geometry got the best of both geometries: a thick leading edge and a rather thin body. It allows reducing both drag and distortion. The geometry is again almost axisymmetric.

	(P_1, Q_1)	(P_2, Q_2)	(P_3, Q_3)	(P_4, Q_4)	(P_5, Q_5)	ΔCDI	ΔC_{D_p}
MOEA/D	-0.029, 0.038	0.042, 0.042	-0.270, -0.105	0.054, 0.066	0.033, -0.184	-0.27%	-3.62%

Table 3: Design variables and performance of the best trade-off for the bi-point optimization

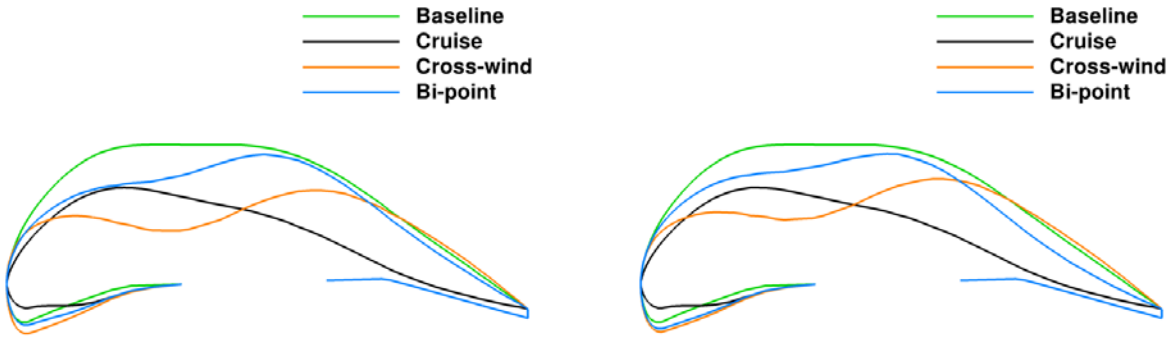

(a) Vertical plane profiles (θ=0° and 180°) (b) Horizontal plane profiles (θ=90° and 270°)

Figure 18. Nacelle profiles resulting from the three optimizations

3. Performance of the best trade-off

The best trade-off nacelle is analyzed in both configurations in Figure 19. In cruise conditions, the shock moves upstream and is stronger as seen in Figure 19(b). The second high speed zone at the middle of the nacelle is also stronger than the cruise optimal nacelle. However the global pressure level remains constant compared to the baseline geometry.

Concerning the cross-wind performance, the two vortices are again visible in Figure 19(d) but the distortion is weaker than for the baseline.

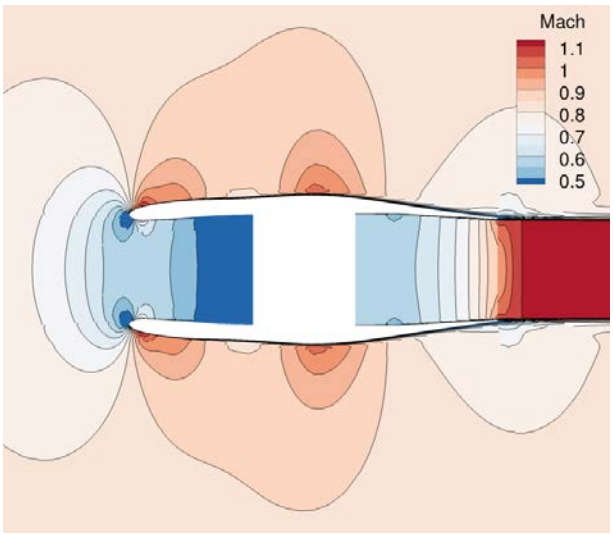

(a) Mach isocontours at cruise conditions of the best trade-off geometry

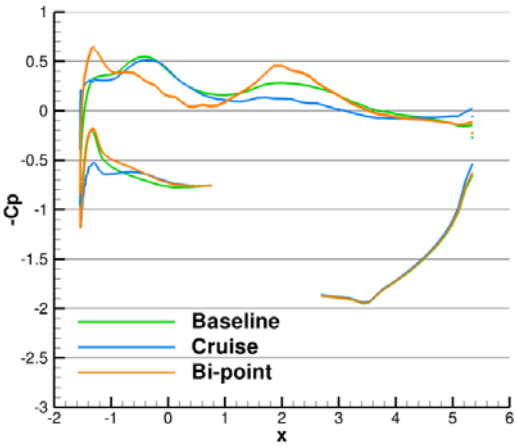

(b) Cp curves comparison between the baseline, the cruise optimal and the best trade-off geometry

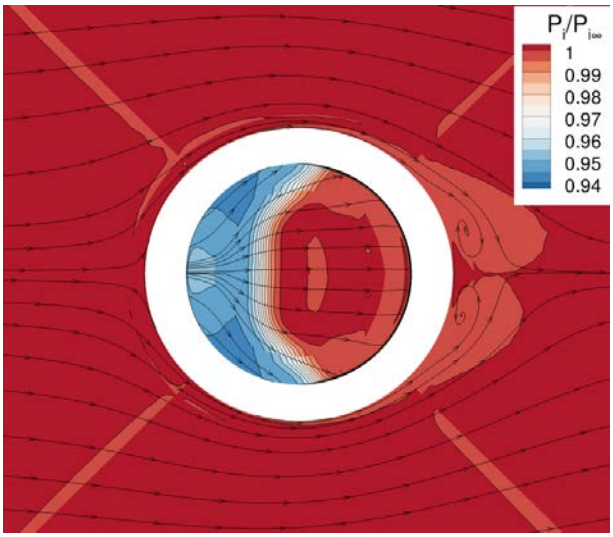

(c) Distortion isocontours at cross-wind conditions of the best trade-off geometry

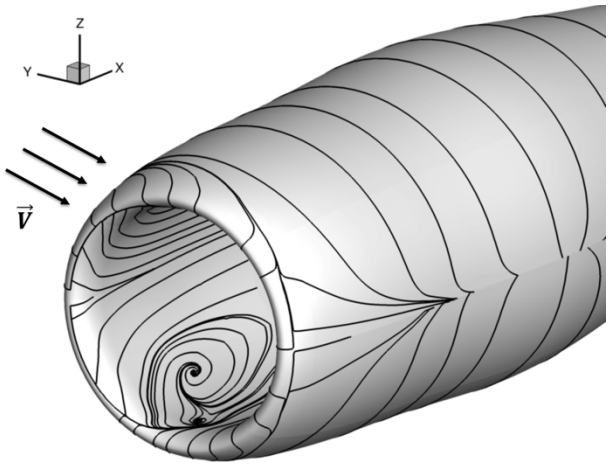

(d) Friction lines at cross-wind conditions of the best trade-off geometry

Figure 19. Performance of the best compromise between cruise and cross-wind requirements

The results of the three optimization processes are summarized in Table 4. The conclusion is that the bi-point optimization succeeded in significantly reducing the distortion index while slightly decreasing the pressure drag coefficient which was already quite low.

	Cruise optimization	**Cross-wind optimization**	**Bi-point optimization**
ΔC_{D_p}	-8.50%	+16.48%	-0.27%
ΔCDI	+0.62%	-6.03%	-3.62%

Table 4: Summary of the three optimizations results

VI. Conclusions and perspectives

Single and bi-point optimizations of an isolated nacelle have been successfully carried out for cruise and crosswind conditions based on high fidelity CFD tools in an automated optimization framework. The various optimization algorithms which have been used have shown their efficiency and the analysis modules their robustness in complex flows calculations for performance and sensitivity assessments. The performance improvement, in terms of drag and flow separation as well as the geometry obtained, has been analyzed and confirms the benefits achieved through the optimizations. In future work the authors plan on integrating a third sizing flight condition: the take-off phase. It is also considered to adapt the engine regime within the CFD computation in order to get a nacelle design optimized for an even more realistic representation of the complete mission. In the prospect of increasing significantly the number of design variables, the functions of interest such as the circumferential distortion index should be adapted to be able to compute adjoint-based sensitivities. To finish, the authors are aware that the resulting geometries are not very realistic and that additional constraints should be added in future work such as volume or structural ones.

Acknowledgments

The authors thank their colleagues from the Applied Aerodynamics Department C. Wervaecke, O. Atinault, A. Dumont for their support in defining the optimization problem and adapting the analyzer.

References

[1] W. Song, A. Keane, "Surrogate-Based Aerodynamic Shape Optimization of a Civil Aircraft Engine Nacelle", *AIAA Journal* 45, 10, 2565-2575, 2007.

[2] D. Sasaki, K. Nakahashi, "Aerodynamic Optimization of an Over-the-Wing-Nacelle-Mount Configuration", *Hindawi Publishing Corporation, Modelling and Simulation in Engineering*, 2011.

[3] P.-A. Lambert, J.-L. Lecordix, V. Braibant, "Constrained Optimization of Nacelle Shapes in Euler Flows using Semianalytical Sensitivity Analysis", *Structural Optimization* 10, 239-246, 1995.

[4] S. Takanashi, "Iterative Three-Dimensional TransonicWing Design Using Integral Equations," *Journal of Aircraft, Vol. 22, No. 8, 1985, pp. 655–660*.

[5] R. Wilhelm, "An Inverse Design Method for Designing Isolated and Wing-Mounted Engine Nacelles", *40th AIAA Aerospace Sciences Meeting & Exhibit*, 2002.

[6] M. Méheut, A. Arntz, G. Carrier, "Aerodynamic Shape Optimizations of a Blended Wing Body Configuration for Several Wing Planforms", 30th AIAA Applied Aerodynamics Conference, 25-28 June 2012, New Orleans, Louisiana, USA.

[7] I. Salah El Din, A. Dumont and C. Blondeau, "Transonic Wing-body Civil Transport Aircraft Aero-Structural Design Optimization using a Bi-Level High Fidelity Approach - A Focus on the Aerodynamic Process", 51st AIAA-ASM, Jan 2013

[8] J.-C. Vassberg et al., "Summary of the Third Drag Prediction Workshop", *AIAA Paper* 2007-0260, January 2007.

[9] Y. Colin, B. Aupoix, J.-F. Boussuge, P. Chanez, "Numerical Simulation of the Distorsion Generated by Crosswind Inlet Flows", *ISABE*, 2007.

[10] http://www.vrand.com/DOT.html

[11] http://dakota.sandia.gov.

[12] N. Hansen, "The CMA Evolution Strategy: A Tutorial", http://www.lri.fr/hansen/cmatutorial.pdf, 2011.

[13] H. Li, Q. Zhang, "Multiobjective Optimization Problems with Complicated Pareto Sets, MOEA/D and NSGA-II", *IEEE Transactions on Evolutionary Computation* 13, 2009.

[14] Cambier L., Veuillot J.-P., "Status of the elsA Software for Flow Simulation and Multi-Disciplinary Applications", *46th AIAA Aerospace Sciences Meeting and Exhibit, Reno, Nevada,* Jan. 2008.

[15] J. Peter, " Discrete Adjoint Method in elsA (part 1): Application to Aerodynamic Design Optimisation. ", *ONERA DLR Aerospace Symposium*, February 2006.

[16] Van der Vooren, J., Destarac, D., "Drag / Thrust Analysis of Jet-Propelled Transonic Transport Aircraft: Definition of Physical Drag Components," *Aerospace Science and Technology*, Vol. 8, No. 7, October 2004.